ISSN:3007-9640 DOI: https://doi.org/10.70114/acmsr.2025.2.1.P221

Bayesian Networks Based Health Assessment for Inertial Sensors of Drag-Free Satellites

Junyang Pan [1, a], Xiaokui Yue [1, b], Zhaohui Dang [1, b] *, and Yibo Ding [1, c]

[1] School of Astronautica, Northwestern Polytechnical University, Xi'an, 710072, China;

[a] junyang_pan@163.com; [b] dangzhaohui@nwpu.edu.cn

Abstract. This paper presents a real-time health assessment model for inertial sensors in drag-free satellites, utilizing Bayesian networks. Initially, a working model of the inertial sensor system for drag-free satellites is developed. Typical faults across various subsystems are identified and used to construct a fault-specific Bayesian network. Subsequently, a fault classification and isolation method is applied, allowing for the rapid identification of subsystem faults by comparing the actual system's inputs and outputs with those predicted by the physical model. Finally, expert knowledge is combined with data-driven techniques to train the structure of different Bayesian network types. Maximum likelihood estimation is employed to determine the Bayesian network parameters, culminating in a comprehensive health assessment model for the inertial sensors of drag-free satellites. Simulation results demonstrate the model's accuracy and effectiveness.

Keywords: Drag-free Satellite; Inertial Sensors; Bayesian Network; Health Assessment.

1. Introduction

The growing demand for stability in space science missions has positioned drag-free spacecraft technology as a pivotal solution for executing high-precision scientific endeavors, such as space-based gravitational wave detection[1,2]. Drag-free satellites utilize high-precision displacement sensors to monitor the relative displacement between the satellite and the test mass, with this data subsequently relayed to the control system[3]. By precisely controlling external thrusters to generate thrust, these satellites can counteract environmental disturbances and minimize noise, thereby establishing an exceptionally low-noise and low-gravity disturbance environment for the entire satellite system, ultimately enabling drag-free motion. However, the intricate and unpredictable nature of the space environment in which drag-free satellites operate, coupled with the complex structure, harsh operational conditions, and numerous unidentified interferences of critical subsystems like the inertial sensor system, make these satellites susceptible to failures. This underscores the necessity for timely health assessments to mitigate equipment degradation and reduce operational costs[4,5]. Despite this, research on health assessment methodologies for drag-free systems remains relatively sparse, particularly in the context of sensor health evaluations[6]. Consequently, conducting comprehensive research on health assessment techniques for drag-free satellite sensors is crucial for enhancing the reliability of spacecraft operations and advancing drag-free technology[7].

The core of spacecraft health assessment methods is the comprehensive analysis of equipment status using both monitoring and historical data[8]. Various approaches are currently employed for this purpose, including the Analytic Hierarchy Process (AHP), the Fuzzy Evaluation Method, Artificial Neural Networks (ANN), and Bayesian network-based techniques[9,10]. AHP quantifies qualitative factors by representing complex problems in a hierarchical structure and assigning initial weights to evaluation indices within the same level, thus minimizing subjective biases and enhancing scientific rigor[11-13]. The Fuzzy Evaluation Method utilizes a defined set of assessment factors, a judgment set, and a fuzzy evaluation matrix, applying fuzzy operators to perform transformations that yield comprehensive assessment outcomes[14-16]. ANN-based methods automatically evaluate spacecraft health by training neural networks on feature information extracted from historical data[17,18].In contrast, Bayesian network-based methods construct health assessment models according to the structure of the target system and employ state data from network nodes for parameter learning, thereby facilitating effective spacecraft maintenance[19-21].

ISSN:3007-9640 DOI: https://doi.org/10.70114/acmsr.2025.2.1.P221

In practical applications, the parameter selection and weight assignment in AHP and the Fuzzy Evaluation Method are still heavily influenced by subjective factors. Moreover, the computational complexity of ANN-based approaches can pose challenges for real-time decision-making in space missions[22]. As a mainstream artificial intelligence framework for representing and reasoning about uncertainty, Bayesian networks effectively integrate domain expertise with data-driven insights. They are widely considered the most robust theoretical model for uncertain knowledge representation and inference. Given the extensive expert experience in drag-free satellite health assessments and the anticipated abundance of on-orbit data, Bayesian network-based methods offer a highly suitable solution for evaluating the health of inertial sensors in drag-free satellites.

Currently, Bayesian network-based methods primarily construct health assessment frameworks by combining expert knowledge with data-driven insights. One such study[23] introduces a digital twin model built on a non-parametric Bayesian network to illustrate both the dynamic degradation of health status and the propagation of cognitive uncertainty. It further proposes a real-time model updating strategy that leverages an improved Gaussian particle filter and a Dirichlet process mixture model, thereby enhancing the adaptability of the digital twin.

In another investigation[24], researchers exploit the modeling capabilities and inference mechanisms of dynamic Bayesian networks to develop an innovative method for fault detection, identification, and recovery in autonomous spacecraft. A separate study[25] employs particle filtering as the inference algorithm for dynamic Bayesian networks, substantially reducing the update time and enabling more efficient health monitoring of aircraft wings.

Additionally, one approach[26] uses Support Vector Machines to track and analyze satellite monitoring and space environment data. The outcomes of various data events are fed into Bayesian fusion nodes, ultimately generating satellite health assessment results at a certain confidence level through data fusion, anomaly event evaluation, and comprehensive processing. Furthermore, researchers[27] have proposed a software and sensor health management system based on Bayesian networks, capable of monitoring the health status of onboard software and sensor systems and achieving onboard diagnostic reasoning.

Lastly, another proposal[28] integrates node fault diagnosis performance data with domain expert judgments to introduce a novel method for parameter specification in Bayesian networks. By analyzing data from a formation flying architecture, this research verifies the effectiveness of the Bayesian network-based fault diagnosis and health monitoring model.

This paper presents a real-time health assessment strategy for inertial sensors in drag-free satellites. Specifically, we propose a Bayesian network structure learning method that integrates expert knowledge with data-driven techniques. By separately training the directed edges of different Bayesian network topologies, the proposed approach effectively consolidates prior expert insights with in-orbit data, substantially improving training efficiency. Ultimately, we employ maximum likelihood estimation to derive the model parameters, thus establishing a robust Bayesian network-based health assessment model for inertial sensors in drag-free satellites.

2. Related Models

In order to conduct further research on the Bayesian network health assessment model, it is essential to first construct a drag-free satellite inertial sensor model and define typical faults for its various subsystems. Subsequently, based on the established inertial sensor fault model, a corresponding typical fault Bayesian network should be developed to support subsequent health assessment procedures.

2.1 Model of Inertial Sensors for Drag-Free Satellites

A drag-free satellite's inertial sensor generally comprises a mechanically sensitive probe, a test mass block, a six-degree-of-freedom capacitive displacement sensing circuit, and an electrostatic feedback control actuator circuit. It operates in two modes: accelerometer mode and inertial

ISSN:3007-9640 DOI: https://doi.org/10.70114/acmsr.2025.2.1.P221
reference mode[29]. Fig. 1provides a basic configuration diagram of the inertial sensor, illustrating its main components and their interconnections.

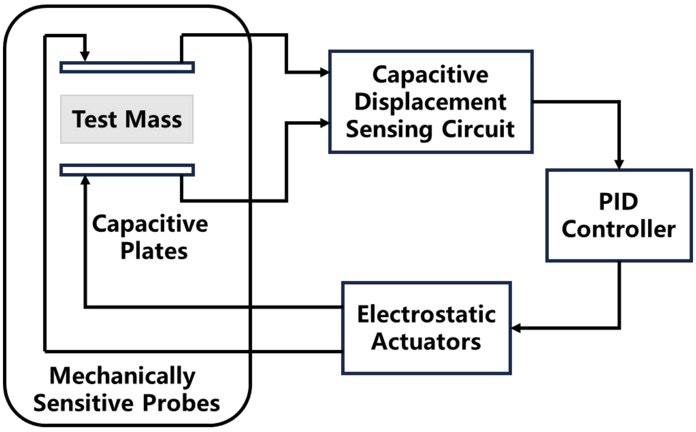

Fig. 1 Schematic diagram of the basic components of inertial sensors

This paper focuses on the inertial sensor[30] operating in the accelerometer mode and subsequently models each of its subsystems as follows.

2.2 Mechanical Sensitive Probe Model

According to the basic principle of parallel plate capacitors and ignoring edge effects, the capacitance C can be expressed as follows:

$$C = \frac{\varepsilon_0 \varepsilon_r A}{d} \tag{1}$$

where ε_0 is the vacuum permittivity, $8.85\times10^{-12}\,\mathrm{F/m}$; ε_r is the relative permittivity related to the material properties; A denotes the effective electrode area; d is the spacing between the electrodes. Under on-orbit conditions, the medium between the electrodes can be approximated as a vacuum, hence $\varepsilon_r \approx 1$.

Typically, the test mass's position and orientation relative to the electrode cage do not remain in a single configuration; instead, they involve both translational and rotational changes, as illustrated in Fig. 1.

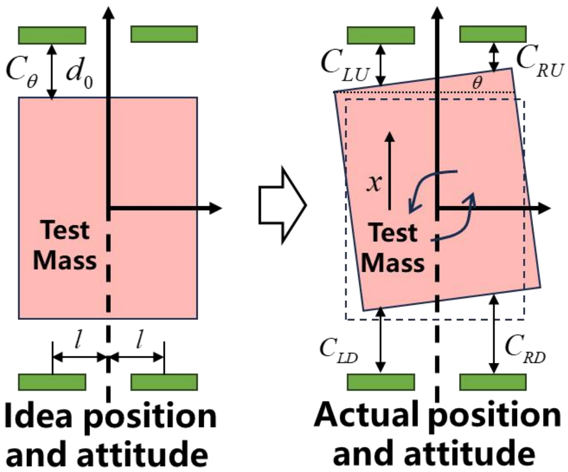

Fig. 1 Actual position and attitude state of the test mass

The change from the ideal to the actual attitude can be decomposed into a combination of translational and rotational movements. Based on this geometric configuration, the differential

ISSN:3007-9640 DOI: https://doi.org/10.70114/acmsr.2025.2.1.P221
capacitance on the left and right electrodes in the actual attitude state can then be derived accordingly.

$$\Delta C_L = C_{LD} - C_{LU} = 2C_0\left(\frac{x}{d_0} - \frac{l\theta}{d_0}\right) \tag{2}$$

$$\Delta C_R = C_{RD} - C_{RU} = 2C_0\left(\frac{x}{d_0} + \frac{l\theta}{d_0}\right) \tag{3}$$

where ΔC_L and ΔC_R are the differential capacitance sizes at the left and right ends of the test mass; d_0 is the spacing between the capacitance plates and the test mass; l is the distance from the center of the capacitor plates to the symmetry plane; x and θ are the displacement and rotation of the test mass relative to the electrode cage. Set the Gaussian noise amplitude of the mechanical sensitive probe to $6.9\times10^{-7}\,\mathrm{pF}\cdot\mathrm{Hz}^{-1/2}$.

2.3 Six-Degree-of-Freedom Capacitive Displacement Sensing Circuit Model

By measuring the differential capacitances on both sides under the actual mixed state, the position and orientation of the test mass relative to the electrode cage can be derived using additive and subtractive algebraic operations. The formula for a specific degree of freedom is provided below, and the same approach applies to other directions. By inverting the aforementioned equations, i.e. Eq.(2) and Eq.(3), the displacement x_f and rotation angle θ_f of the test mass are then obtained:

$$x_f = \frac{d_0(\Delta C_L + \Delta C_R)}{4C_0} \tag{4}$$

$$\theta_f = \frac{d_0(\Delta C_R - \Delta C_L)}{4lC_0} \tag{5}$$

To facilitate the subsequent design of PID control parameters, the attitude information is amplified through a dedicated amplification module. This ensures that the control signals remain within an optimal dynamic range for precise parameter tuning.

$$x_a = c_X x_f \tag{6}$$

$$\theta_a = c_\theta \theta_f \tag{7}$$

where c_X and c_θ reprensent the amplification coefficients; x_a and θ_a denote the amplified displacement and rotation angle signals, respectively. Set the Gaussian noise amplitude of the six-degree-of-freedom capacitive displacement sensing circuit[31] to $1.7\,\mathrm{nm}\cdot\mathrm{Hz}^{-1/2}$.

2.4 Drag-Free Test Mass PID Control Model

Drawing on the inertial sensor structure described in "Tianqin" mission, this study adopts an electrode connection arrangement as the voltage configuration scheme, as illustrated in Fig. 2. From the electrode segmentation and voltage configuration, one can determine the electrostatic force driving approach for each measurement direction. Taking the X direction as an example, the corresponding electrode is divided into three sections (X_1, X_2, X_3), each of which is supplied with a control voltage. To induce translational motion along the X axis, feedback voltages must be applied simultaneously on these three sections, generating electrostatic forces F_{eX1} and F_{eX3} those oppose the inertial forces. In practice, however, perfect synchronization of these three electrode regions is not feasible, and coupling effects arise among them. Consequently, time-sharing control is employed to achieve decoupling[32].

ISSN:3007-9640 DOI: https://doi.org/10.70114/acmsr.2025.2.1.P221

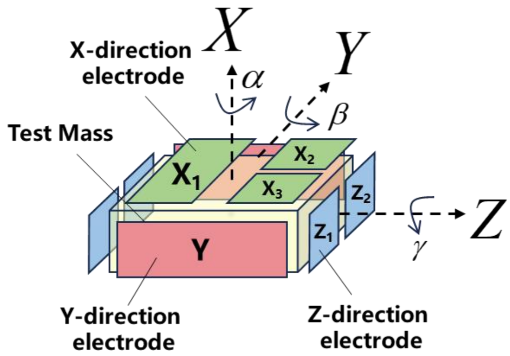

Fig. 2 Electrode connection and merging structure

2.5 Electrostatic Feedback Control Actuator Circuit Model

According to the static and dynamic mechanical models for multi-degree-of-freedom control, once the test mass is regulated to the center of the electrode cage and reaches equilibrium, the electrostatic force and torque acting on it become equal to the inertial force and torque, as illustrated in Fig. 3. Here, a in it is the acceleration of the test mass.

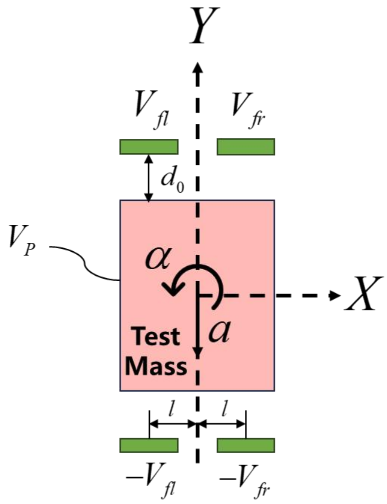

Fig. 3 Test mass electrostatic force model

The relationship between the electrostatic force acting on the test mass and the voltage applied to the electrodes on opposing sides can be described by the following equation:

$$F_{el} = \frac{2\varepsilon_0\varepsilon_r A V_p}{d_0^2} V_{fl} \tag{8}$$

$$F_{er} = \frac{2\varepsilon_0\varepsilon_r A V_p}{d_0^2} V_{fr} \tag{9}$$

where V_p is the surface potential of the test mass; V_{fl} and V_{fr} are the surface potentials of the left and right electrode plates. The linear acceleration and angular acceleration of the test mass are obtained as:

$$a = \frac{F_{el} - F_{er}}{m} = \frac{2\varepsilon_0\varepsilon_r A V_p}{m d_0^2}\left(V_{fl} - V_{fr}\right) \tag{10}$$

$$\alpha = \frac{F_{el}\cdot l - F_{er}\cdot l}{J} = \frac{2\varepsilon_0\varepsilon_r A l V_p}{J d_0^2}(V_{fl} - V_{fr}) \tag{11}$$

ISSN:3007-9640 DOI: https://doi.org/10.70114/acmsr.2025.2.1.P221

Set the Gaussian noise amplitude of the electrostatic feedback control actuator circuit[31] to $1\times10^{-5}\,\mathrm{V/Hz^{-1/2}}$.

2.6 Drag-Free Test Mass Motion Model

The scaling factors for the different axes of a are:

$$K_i = \frac{2\varepsilon_0\varepsilon_r A V_p}{m d_0^2} \qquad (i = X, Y, Z)$$
$$K_j = \frac{4\varepsilon_0\varepsilon_r A l V_r}{J d_0^2} \qquad (j = \alpha, \beta, \gamma) \tag{12}$$

The motion model of drag-free test mass satisfy the following equation:

$$\begin{aligned} \ddot{x} &= K_X\left(V_{X_1}+V_{X_2}+V_{X_3}\right) \\ \ddot{y} &= K_Y V_Y \\ \ddot{z} &= K_Z(V_{Z_1}+V_{Z_2}) \\ \ddot{\alpha} &= K_\alpha(V_{Z_2}-V_{Z_1}) \\ \ddot{\beta} &= K_\beta(V_{X_2}-V_{X_3}) \\ \ddot{\gamma} &= K_\gamma\left(V_{X_1}-V_{X_2}-V_{X_3}\right) \end{aligned} \tag{13}$$

where V_i is the voltage applied to the electrode surface. Set the surface potential of the test mass in the accelerometer mode to 5V, the Gaussian noise amplitude of the acceleration disturbance to $1\times10^{-7}\,\mathrm{m/s^2}$, and the Gaussian noise amplitude of the surface potential[33] to $100\,\mathrm{mV}$.

2.7 Typical Fault Design

The inertial sensor system encompasses nine distinct fault types, as summarized in Table 1:

Table 1. Typical fault types of subsystems

Subsystem	Typical Fault Types
Capacitive Displacement Sensing Circuit	Signal amplitude distortion Signal interruption Signal delay
PLC Circuit	1. Signal interruption
Feedback Control Mechanism	Signal amplitude distortion Signal interruption Signal delay
UV Discharge Device	Deviation fault Instability fault

The specific forms of different types of faults are as follows.

(1) Amplitude distortion is:

$$u = k \cdot u \tag{14}$$

where u is the input signal, and k ($k\neq0$) is the amplitude distortion coefficient.

(2) Signal interruption: The output remains constantly at zero.

(3) Signal delay: The output signal lags the input by n discrete time steps.

(4) Deviation fault: A discrepancy arises between the test mass surface potential and the designated (reference) potential.

(5) Instability fault: Due to uncontrollable noise or changes in the ultraviolet (UV) discharge device, DC motor, or other components, the potential of the test mass fluctuates over time.

ISSN:3007-9640 DOI: https://doi.org/10.70114/acmsr.2025.2.1.P221

2.8 Typical Fault Bayesian Network

By integrating the actual inertial sensor model with the typical fault design, we obtain the Bayesian network structure diagram of these typical faults, as illustrated in Fig. 4.

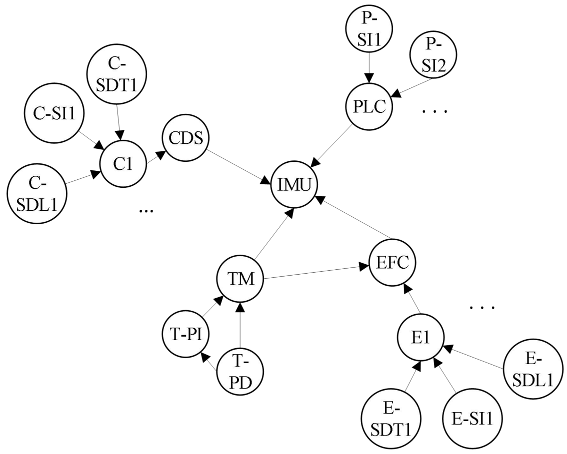

Fig. 4 Bayesian network structure diagram of typical faults

In this figure, CDS denotes the capacitive displacement sensing circuit, TM denotes the test mass, EFC represents the electrostatic feedback controller, PLC indicates the PID controller module, and IMU stands for the inertial reference sensor. The symbols C_i and E_i refer to sub-models corresponding to a certain degree of freedom within the relevant subsystem. Meanwhile, SDT indicates amplitude distortion, SDL indicates signal interruption, PD denotes a deviation fault, and PI denotes an instability fault.

For different fault root nodes and their associated system state child nodes, the designed node states are listed in Table 2.

Table 2. Node State Design

Node Name	Node States
IMU	Fully healthy (0), Relatively healthy (1), General (2), Abnormal (3), Fault (4)
CDS	Fully healthy (0), Relatively healthy (1), General (2), Abnormal (3), Fault (4)
TM	Healthy (0), General (1), Fault (2)
EFC	Fully healthy (0), Relatively healthy (1), General (2), Abnormal (3), Fault (4)
PID	Healthy (0), Fault (1)
X-SDT	None (0), Slight (1), Severe (2)
X-SI	None (0), Severe (1)
X-SDL	None (0), Slight (1), Severe (2)
PD	None (0), Slight (1), Severe (2)
PI	None (0), Slight (1), Severe (2)

The specific values for different states of the fault root node are listed in Table 3:

Table 3 Fault state values

Node Name	None (0)	Slight (1)	Severe (2)
X-SDT	0.9~1.1	0.8~0.9 and 1.1~1.2	$<$0.8 and $>$1.2
X-SI	1	-	0
X-SDL	0	1~3	3~5
PD	4.5~5.5	4~4.5 and 5.5~6	$<$4 and $>$6
PI	0~0.1	0.1~0.5	$>$0.5

ISSN:3007-9640 DOI: https://doi.org/10.70114/acmsr.2025.2.1.P221

3. Fault Identification Model

To address the coupling issues between faults and across subsystems, a classification-based approach is employed to achieve decoupling. By comparing discrepancies between the outputs of the actual system and those predicted by the physical model, fault identification schemes tailored to different fault types are designed, enabling rapid detection of subsystem faults.

3.1 Fault Identification Signal Acquisition

To facilitate subsequent fault identification, input and output signals from each subsystem are gathered, as illustrated in Fig. 5. Specifically, based on the inertial sensor's subsystem structure, the following fault identification signals are collected: the differential capacitance between the plates, the test mass's displacement and angle errors, the feedback control voltage, the actual plate surface voltage, and the test mass surface potential.

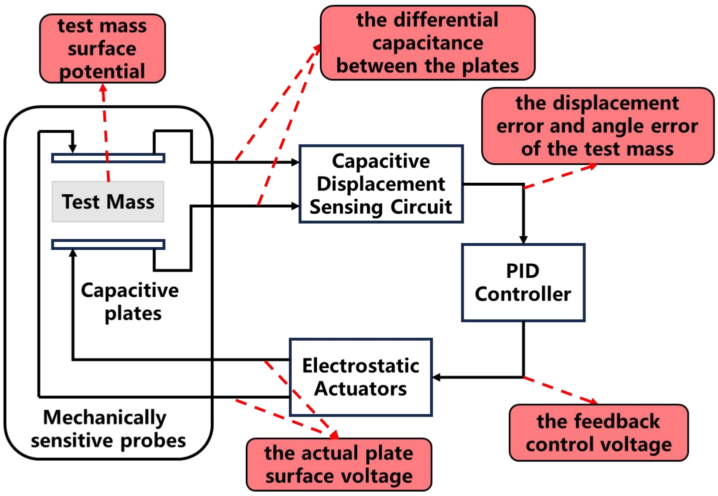

Fig. 5 Schematic of Fault identification signal acquisition

3.2 Fault Identification Method

To address the coupling among signal amplitude faults and signal interruption and delay faults, we first isolate the signal amplitude fault from the signal interruption and delay faults. Next, based on the subsystem input and output signals, a delay counter is employed to determine the statuses of the signal interruption and delay fault root nodes. The signal amplitude fault root node status is obtained by comparing the actual system outputs with the physical model outputs. The overall fault identification process is shown in Fig. 6. By default, if an interruption fault occurs, the statuses of the other two fault root nodes are both set to 0.

First, the delay counter limit value is set to 5, referencing the signal delay fault state values in Table 3. Next, based on the subsystem's input and output signals, the statuses of the delay fault root node and the interruption fault root node are determined by using the delay counter. Afterward, depending on the delay fault status, the synchronous storage signal corresponding to the actual input and output signals is extracted. Finally, by comparing the actual system outputs with those of the physical model, the amplitude fault root node status is established.

For deviation faults and instability faults, the deviation between the test mass surface potential and the given potential, as well as the extent of its temporal variation, are obtained within a specified time range. These measurements determine the status of the deviation fault root node and the instability fault root node.

ISSN:3007-9640 DOI: https://doi.org/10.70114/acmsr.2025.2.1.P221

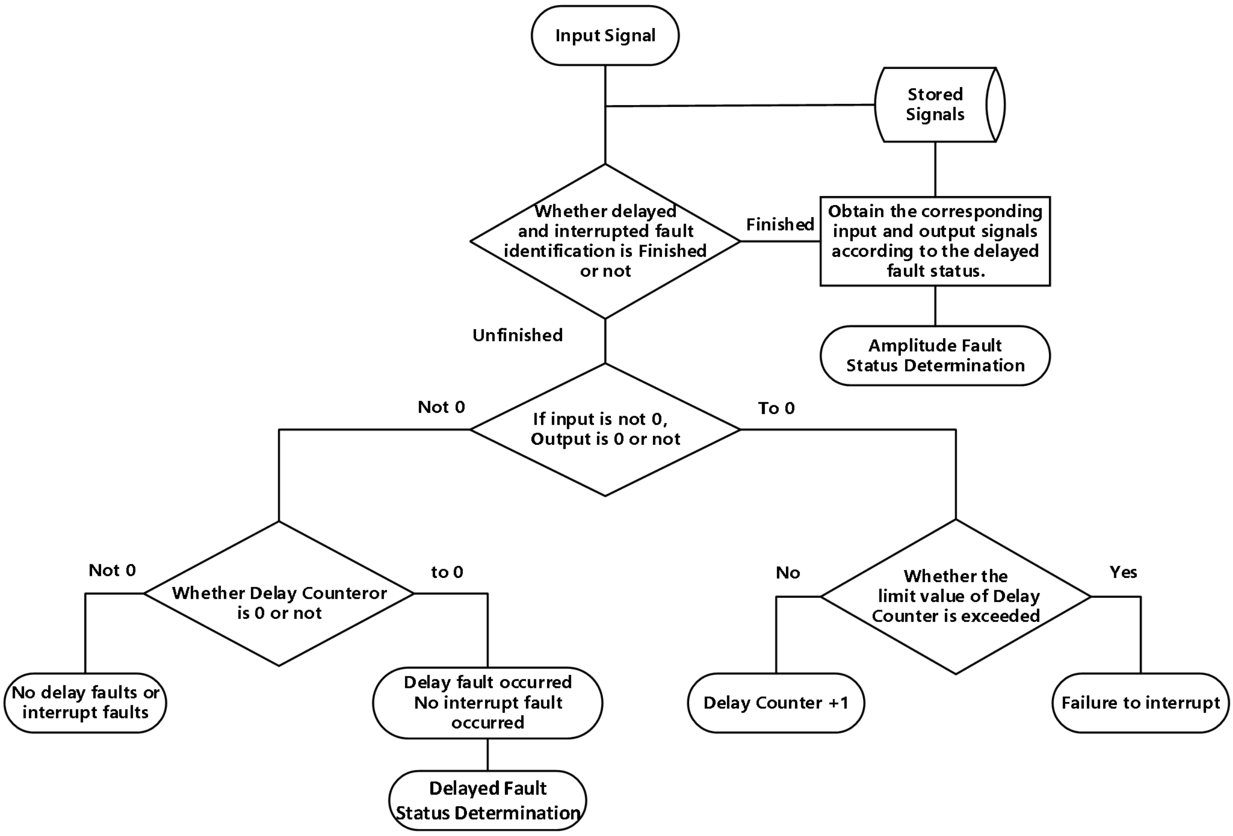

Fig. 6 Signal interruption, delay, and amplitude fault identification process

Deviation fault and instability fault identification methods are as follows:

$$PD = \frac{\sum_{i=0}^{N} \left| V_p - \overline{V}_i \right|}{n} \tag{15}$$

$$PI = \frac{\sum_{i=0}^{n-1} \left| \overline{V}_{i+1} - \overline{V}_i \right|}{n-1} \tag{16}$$

where $\overline{V}_i$ is the measured test mass surface potential.

For the fault coupling issues between subsystems, those with coupling relationships are identified sequentially according to the signal flow, as illustrated in Fig. 7. The fault identification signals, along with the fault status of the upstream subsystems, are applied to determine the fault status of the current subsystem. By default, if an interruption fault occurs in one subsystem, the corresponding node statuses in any subsequent subsystem models are all set to 0.

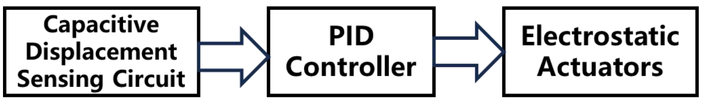

Fig. 7 Coupling subsystem fault identification order

3.3 Fault Dataset Generation

To facilitate further research on the Bayesian network health assessment model, we employ the typical fault Bayesian network, sensor fault model, and fault identification model to derive a Bayesian network fault dataset, as illustrated in Fig. 8.

ISSN:3007-9640 DOI: https://doi.org/10.70114/acmsr.2025.2.1.P221

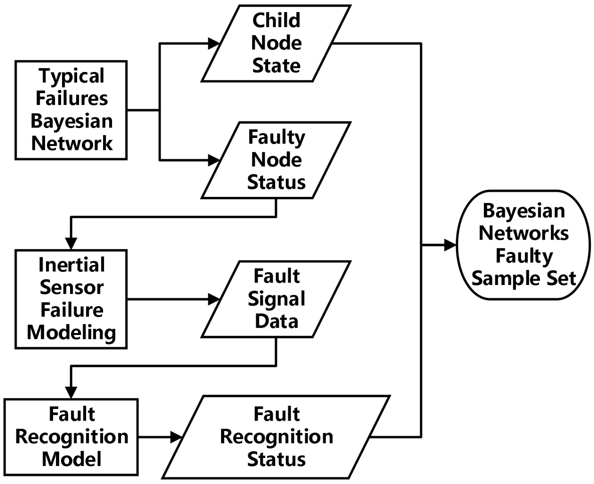

Fig. 8 Fault dataset generation

First, 10,000 fault samples are randomly generated using the typical fault Bayesian network. These samples are then partitioned into fault root node statuses and child node statuses, yielding the actual fault root node status set and the child node status set. Next, based on the actual fault root node status set, a fault signal dataset is produced by applying the inertial sensor fault model. Finally, the fault signal dataset undergoes fault identification via the fault identification model, resulting in an identified fault root node status set. This identified set is then combined with the child node status set to form the complete Bayesian network fault sample set.

4. Bayesian Network Health Assessment Model

A Bayesian network approach is employed to build a health assessment model for the inertial sensors of drag-free satellites. Specifically, the fault sample set derived from the fault identification model is used to train the Bayesian network, enabling determination of its structure and conditional probability tables. This process ultimately yields a Bayesian network-based health assessment model for the inertial sensors.

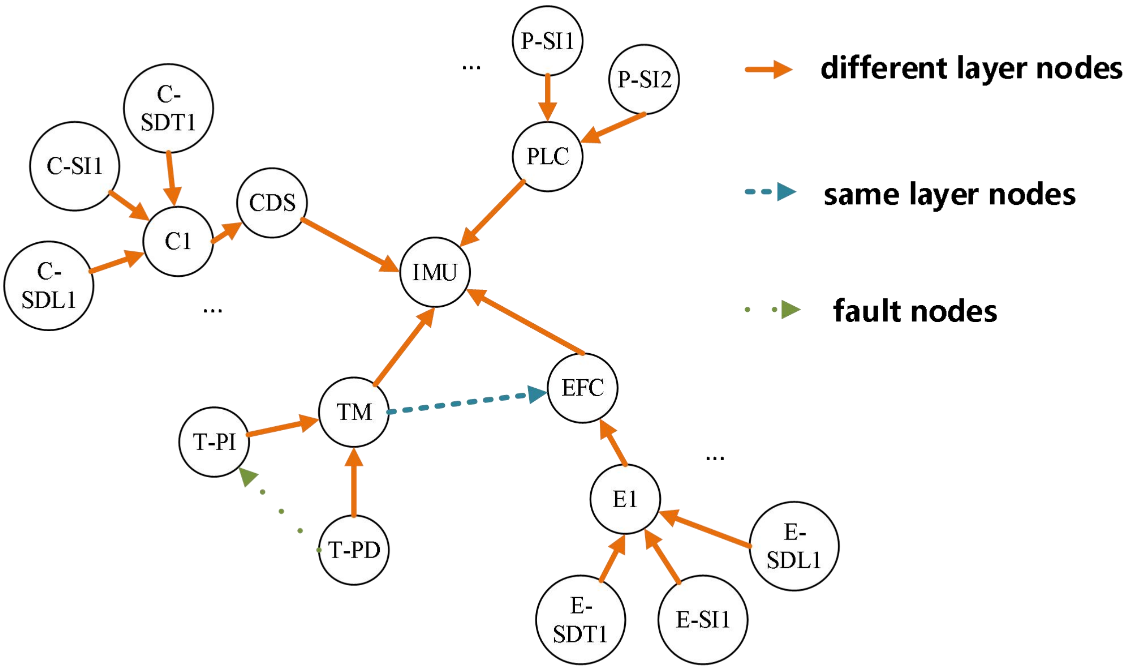

Fig. 9 Division of node-directed edges in the Bayesian network

ISSN:3007-9640 DOI: https://doi.org/10.70114/acmsr.2025.2.1.P221

4.1 Bayesian Network Structure Training

To accelerate Bayesian network structure training and enhance its accuracy, the network's directed edges are categorized into three groups: edges connecting different layers of nodes, edges connecting nodes within the same layer, and edges connecting fault nodes. Specific structural training methods are designed for each category, thereby determining the node's connections and directional relationships. The partitioning of node-directed edges in the network is shown in Fig. 9.

4.1.1 Directed Edges Between Different Layer Nodes

Since the relationships between nodes in different layers are relatively straightforward, we assign the edges and directions between these nodes in the Bayesian network in advance, based on the inertial sensor system's fault tree. The fault tree of the inertial sensor system is illustrated in Fig. 10.

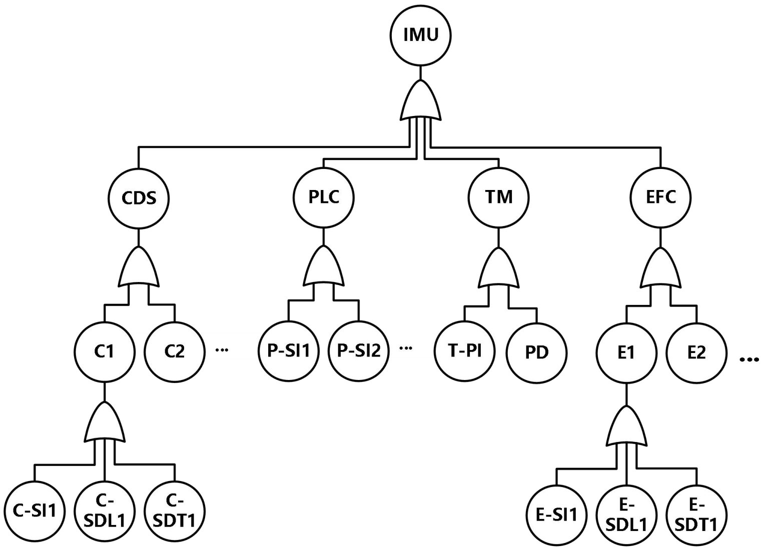

Fig. 10 Fault tree of the inertial sensor system

Based on the hierarchical relationships in the fault tree, the corresponding nodes in the Bayesian network are connected with directed edges, yielding the initial network structure shown in Fig. 11.

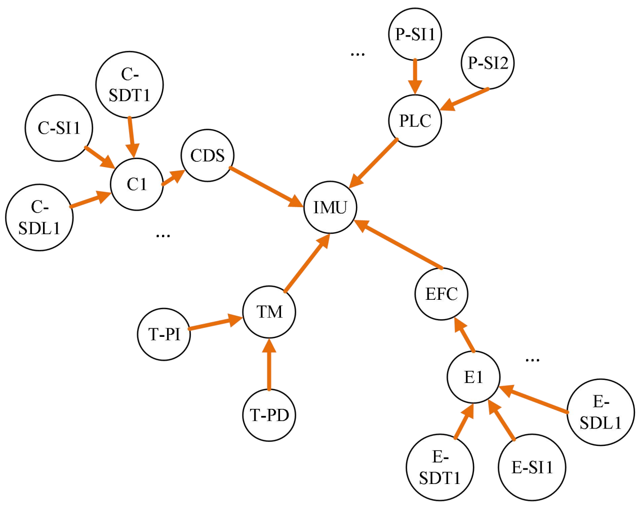

Fig. 11 Initial Bayesian network structure

4.1.2 Directed Edges Within the Same Layer Nodes

Because the relationships among nodes in the same layer are relatively unclear, we employ Dempster's rule[34] of combination to synthesize multiple expert's opinions. This approach

ISSN:3007-9640 DOI: https://doi.org/10.70114/acmsr.2025.2.1.P221
effectively integrates expert prior knowledge and yields the edges and directions among nodes within the same layer. The resulting structure is illustrated in Fig. 12.

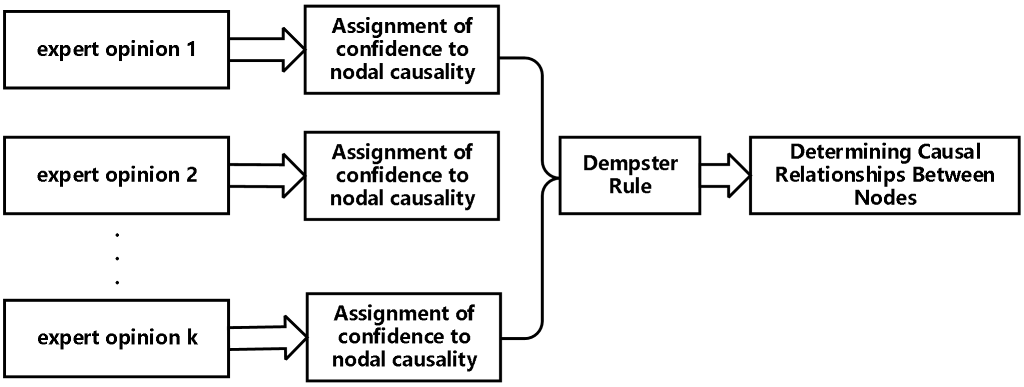

Fig. 12 Determination process of nodes within the same layer

It is stipulated that each set of variables includes two nodes within the same layer, X_a and X_b. $X_a \to X_b$ indicates that the expert believes there is a directed edge from X_a to X_b. $X_b \to X_a$ indicates that the expert believes there is a directed edge from X_b to X_a. $X_a \not\leftrightarrow X_b$ indicate that the expert believes there is no direct dependency between X_a and X_b. Suppose there are k experts, and the corresponding belief assignment table is shown in Table 4. E_i represents the opinion of the i-th expert, and $v_i(\varphi_i)$ represents the confidence distribution of event φ_i in the opinion of the i-th expert. The hypothesis with the highest belief measure is selected as the causal relationship among nodes within the same layer and is then integrated into the initial Bayesian network structure, yielding the updated Bayesian network structure shown in Fig. 13.

Table 4 Expert opinion belief assignment

	$X_a \to X_b$	$X_b \to X_a$	$X_a \not\leftrightarrow X_b$
E_1	$v_1(\varphi_1)$	$v_1(\varphi_2)$	$v_1(\varphi_3)$
E_2	$v_2(\varphi_1)$	$v_2(\varphi_2)$	$v_2(\varphi_3)$
…	…	…	…
E_k	$v_k(\varphi_1)$	$v_k(\varphi_2)$	$v_k(\varphi_3)$
Sum	$v(\varphi_1)$	$v(\varphi_2)$	$v(\varphi_3)$

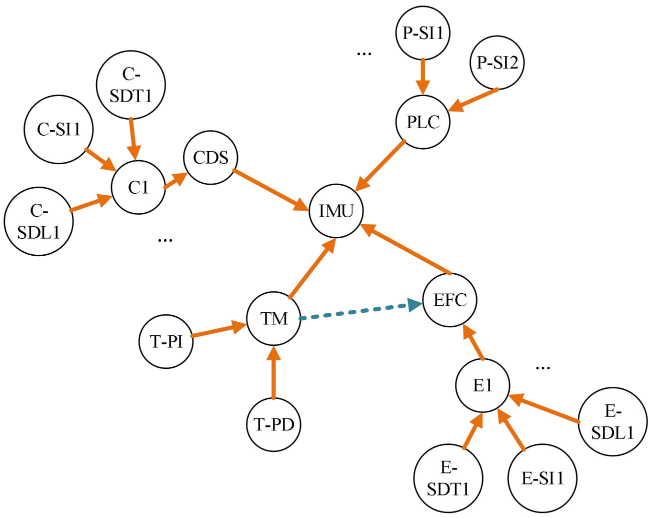

ISSN:3007-9640 DOI: https://doi.org/10.70114/acmsr.2025.2.1.P221

Fig. 13 Progressive Bayesian network structure

4.1.3 Directed edges of fault nodes

Because the relationships among fault nodes are not clearly defined and prior knowledge is limited, we employ a data-driven method based on the PC algorithm[35] to learn the edges and directions among nodes using the fault sample set. To further speed up computation, the fault nodes are grouped according to different sub-models and solved separately. This partitioning of fault nodes is shown in Fig. 14.

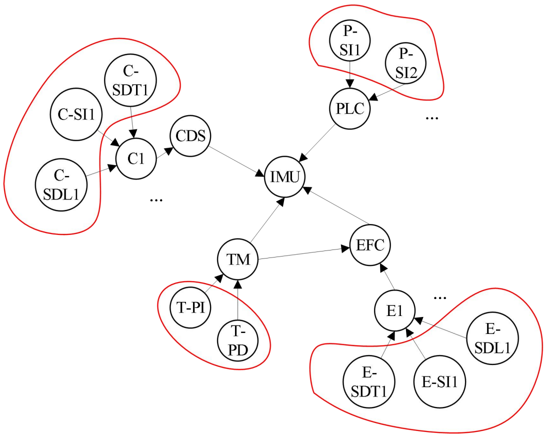

Fig. 14 Fault node division diagram

Since, during the fault identification process, the occurrence of signal interruption faults can complicate the identification of signal delay and amplitude distortion faults, and once a signal interruption fault occurs, the inertial sensor system immediately transitions to a fault state, the connections between signal interruption faults and other fault types are disregarded. The directed edges of fault nodes obtained through this process are then integrated into the refined Bayesian network structure, resulting in the complete Bayesian network structure shown in Fig. 15.

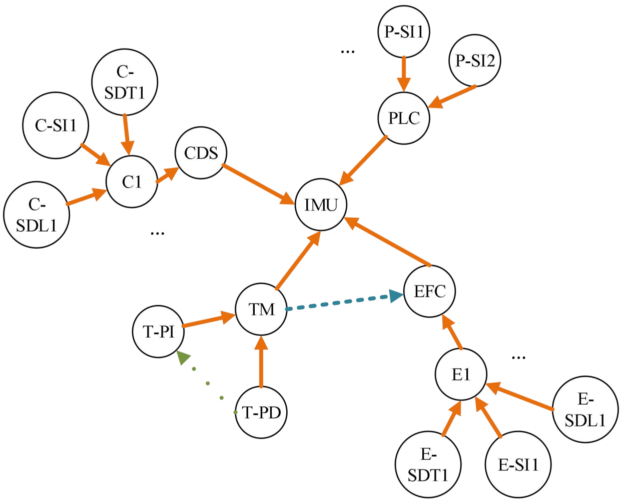

Fig. 15 Complete Bayesian network structure

4.2 Bayesian Network Parameter Estimation and Inference

Since the maximum likelihood estimation (MLE) method can obtain an unbiased estimate of the original distribution when sufficient data is available, it is chosen as the parameter estimation method for the Bayesian network.

The conditional probability of a random variable in the Bayesian network taking a specific value is defined as follows:

ISSN:3007-9640 DOI: https://doi.org/10.70114/acmsr.2025.2.1.P221

$$P(x)=\prod_{i}^{n}P(X_i\mid\pi_i;\theta_i) \tag{17}$$

where $x=\{X_1,X_2,\cdots,X_n\}$ is a multivariate random variable; π_i is the set of parent nodes of X_i; θ_i is the conditional probability distribution table of the random variable X_i.

The log-likelihood function of the maximum likelihood estimation is:

$$l(\theta\mid D)=\sum_{l=1}^{m}\ln P(D_l\mid\theta) \tag{18}$$

where $D=\{D_1,D_2,\cdots,D_m\}$ is the data sample set.

By maximizing the log-likelihood function, the maximum likelihood estimates of the conditional probability tables (CPTs) are obtained, thereby establishing the parameters of the Bayesian network.

The belief propagation algorithm[36] is an exact inference method designed for Bayesian networks with tree structures. This algorithm leverages the conditional independence between variables and the distributive properties of sum and product operations, allowing the global summation to be confined to local regions. Consequently, this significantly simplifies the computational process.

Given the real-time inference requirements for the on-orbit health assessment of drag-free satellites, the belief propagation algorithm is selected as the inference method for the Bayesian network to enhance its inference speed and efficiency.

5. Simulation Results

5.1 Simulation Settings

The simulation sampling interval is set to 0.01 seconds to accurately capture the system dynamics. The relevant parameters of the test mass are listed in Table 5.

Table 5 Test mass related parameters

Type	Value
Mass/ (kg)	0.072
Moment of Inertia/ $(kg\bullet m^2)$	$\lfloor\ 0 \quad 0 \quad 10.2\ \rfloor$
Initial Position Range/ (m)	$[2\times10^{-6}\sim10\times10^{-6}]$
Initial Angle Range/ $(°)$	$[1\sim4]$
Initial Velocity Range/ (m/s)	$[-5\sim5]\times10^{-6}$
Initial Angular Velocity Range/ $(°/s)$	$[-2\sim2]$

Set the amplifier module coefficients $c_X=1\times10^6$, $c_\theta=1\times10^3$ .The six-degree-of-freedom PID coefficients are shown in Table 6.

Table 6 PID Coefficients

PID coefficients	x	y	z	w_x	w_y	w_z
proportional	0.05	0.3	0.4	50	1.2	2
integral	0	0	0	0	0	0
derivative	0.02	0.2	0.3	30	0.4	0.8

ISSN:3007-9640 DOI: https://doi.org/10.70114/acmsr.2025.2.1.P221

5.2 Fault Identification Model Sensitivity Test

To facilitate the subsequent comparison of fault simulations and assess the stability of the PID controller, set the simulation time to 5s, and the test mass-related parameters are shown in Fig. 16.

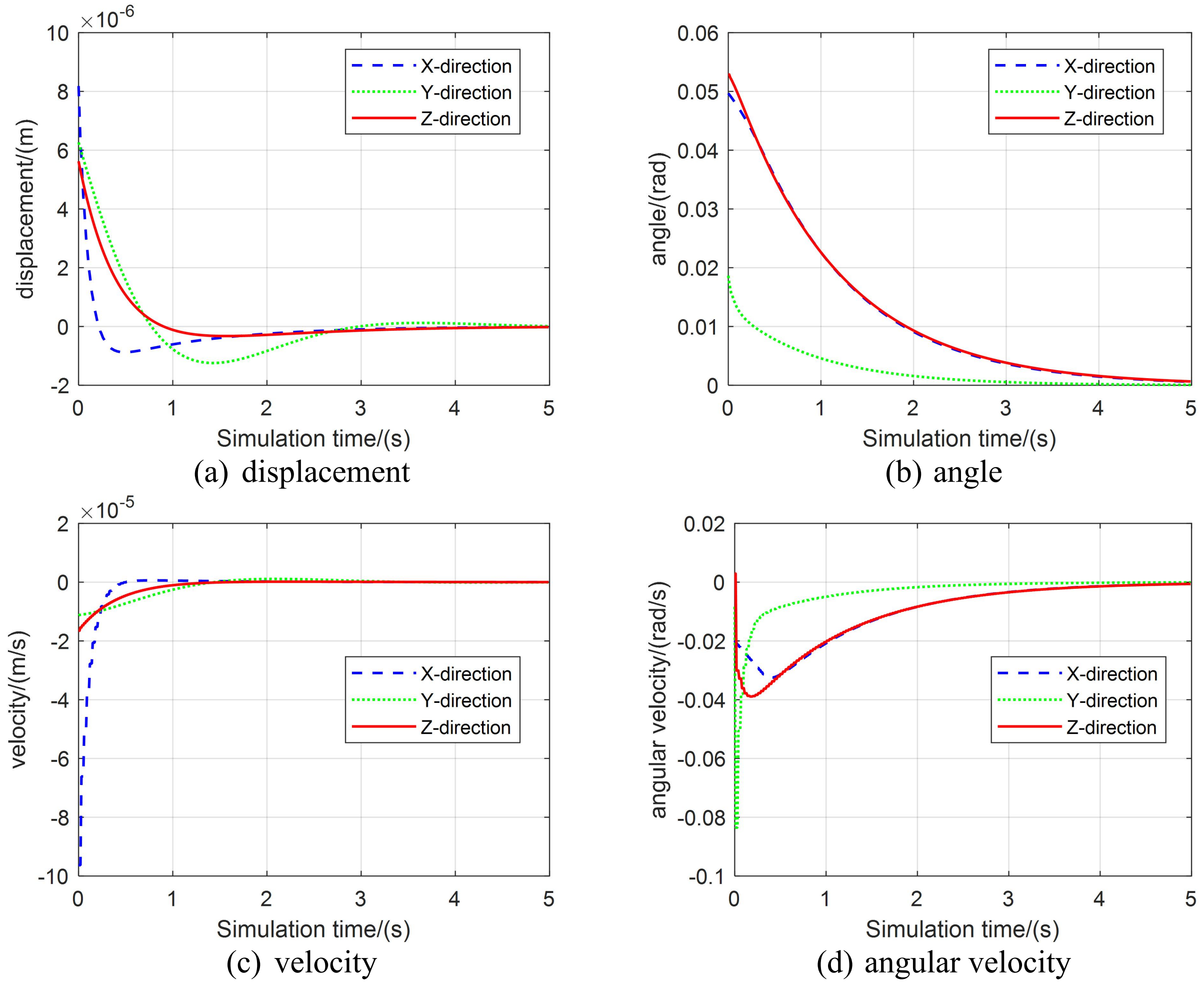

(a) displacement (b) angle

(c) velocity (d) angular velocity

Fig. 16 Simulation results of test mass-related parameters

The simulation results indicate that the time-sharing controlled PID controller effectively addresses the issue of coupling within the control region. It stabilizes the inspection quality in a short period, enabling accurate tracking of the inspection quality without drag in drag-free satellites.

To evaluate the sensitivity of the fault identification model, we subject the capacitive displacement sensing circuit and feedback control mechanism to severe fault conditions. Specifically, the following faults are induced:

a. X-direction signal amplitude distortion fault;
b. Signal delay fault;
c. UV discharge device deviation fault;
d. Instability fault.

Under these severe fault conditions, we obtain the simulation-related parameters, as shown in Fig. 17. The simulation results show that these fault conditions lead to increased overshoot and delay phenomena in the PID controller during the control process. However, the PID controller can still achieve stable control of inspection quality in a short period under fault conditions, exhibiting strong robustness. The time required for the fault identification model to detect various faults is presented in Table 7. The simulation results demonstrate that the fault identification model can quickly and accurately identify different types of faults at their respective locations, effectively mitigating the coupling between faults.

ISSN:3007-9640 DOI: https://doi.org/10.70114/acmsr.2025.2.1.P221

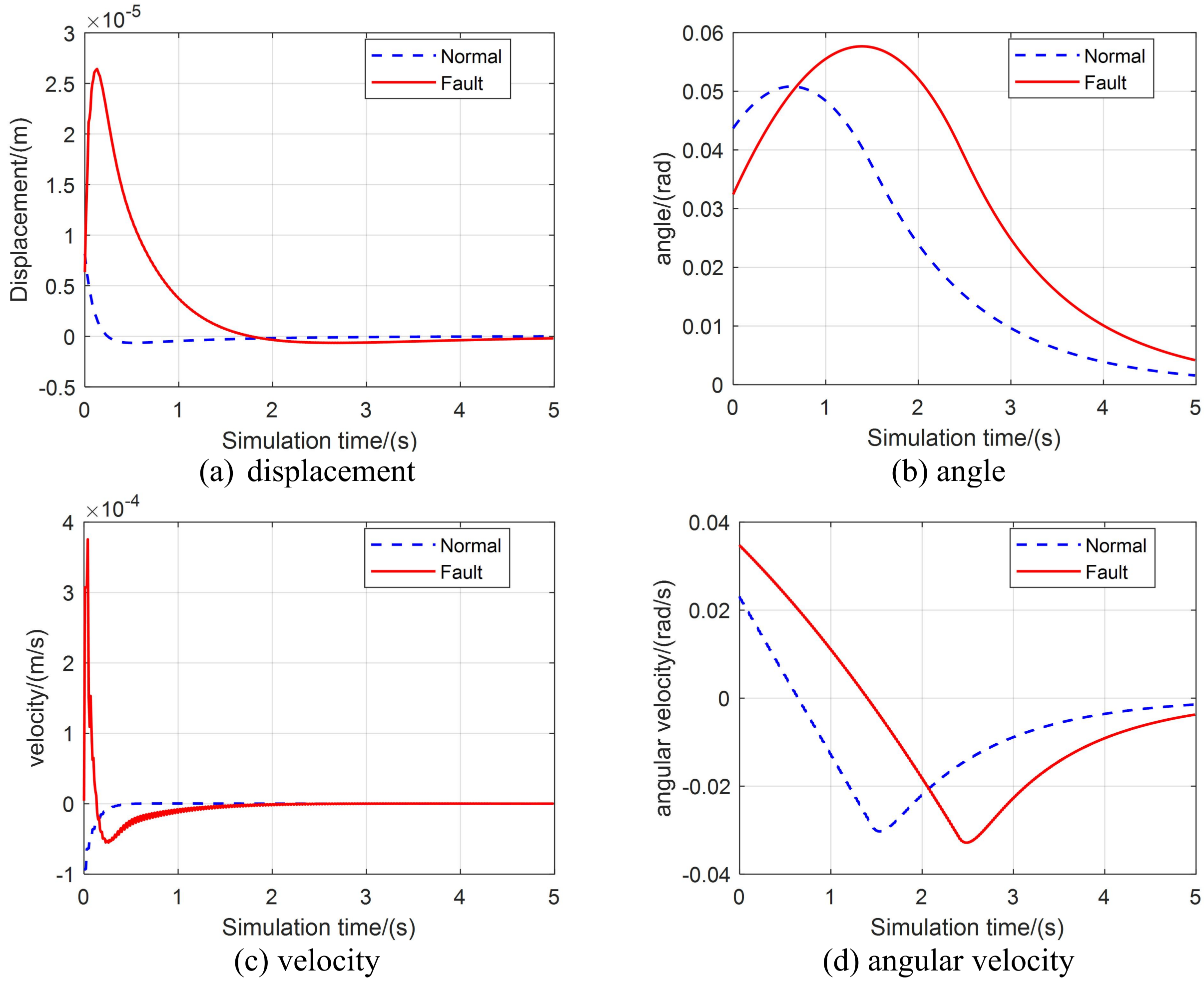

(a) displacement (b) angle

(c) velocity (d) angular velocity

Fig. 17 Simulation results of quality-related parameters under fault conditions

Table 7 Fault Identification Time Table

Fault Types	C-SDT	C-SI	C-SDL	P-SI	E-SDT	E-SI	E-SDL	PD	PI
Time/ (s)	0.05	0.05	0.05	0.07	0.27	0.27	0.27	0.01	0.1

5.3 Bayesian Network Structure Similarity

To construct the Bayesian network-based health assessment model, we first utilize the fault identification model to generate a fault dataset for training the Bayesian network. After training, we evaluate the structural similarity between the trained Bayesian network and the typical fault Bayesian network using the F1-score. The Bayesian network model that has been trained by integrating expert knowledge with data-driven methods is shown in Fig. 18.

The F1-score evaluation scores and simulation times are shown in Table 8. The simulation results show that the trained Bayesian network has a higher structural similarity with the typical fault Bayesian network, and the training speed has been greatly improved, indicating the accuracy and efficiency of the Bayesian network structure learning method that combines expert knowledge and data-driven methods.

ISSN:3007-9640 DOI: https://doi.org/10.70114/acmsr.2025.2.1.P221

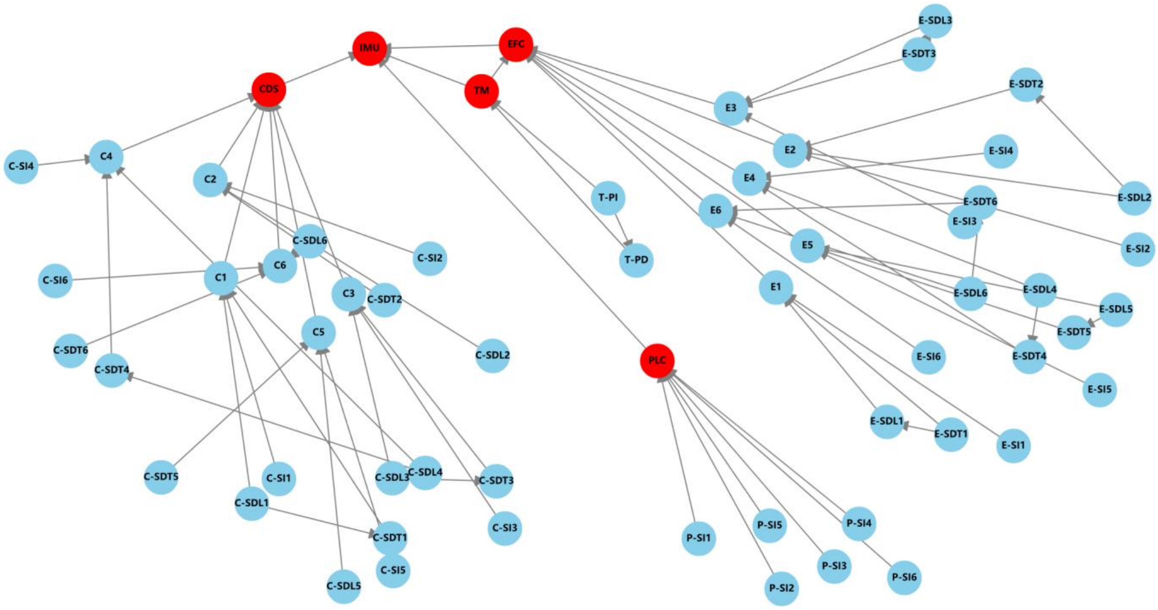

Fig. 18 Proposed Bayesian network model

Table 8. Fault Identification Time

	Expert Knowledge and Data-Driven	PC Algorithm
F1-score	0.93	0.74
Training Time	2s	1min13s

5.4 Bayesian Network Health Assessment Accuracy

To evaluate the accuracy of the Bayesian network's health assessment, 10,000 groups of fault node statuses are randomly generated using the Monte Carlo method, a statistical sampling technique. By comparing the child node statuses inferred by the typical fault Bayesian network with those inferred by the trained Bayesian network, we determine the health assessment accuracy of the Bayesian network. The inference accuracy for different child nodes is presented in Table 9. The simulation results demonstrate that the trained Bayesian network can accurately infer child node states from fault node states, achieving high accuracy in health assessments.

Table 9. Reasoning accuracy of different child nodes

Node Type	Node Accuracy
IMU	0.995
CDS	0.983
TM	0.986
EFC	0.977
PID	0.992

6. Summary

To address the health assessment challenges of inertial sensors in drag-free satellites, we designed a Bayesian network structure training method that integrates expert knowledge with data-driven approaches. This integration resulted in the development of a Bayesian network-based health assessment model. The simulation results lead to the following conclusions. Firstly, the proposed Bayesian network structure training method effectively combines expert prior knowledge with on-orbit data, thereby enhancing both the accuracy and efficiency of the Bayesian network structure. Secondly, the Bayesian network parameter estimation and reasoning methods employed

ISSN:3007-9640 DOI: https://doi.org/10.70114/acmsr.2025.2.1.P221

in this study can accurately assess the health status of the drag-free satellite system and its subsystems based on fault node statuses. In summary, the Bayesian network-based health assessment model for inertial sensors in drag-free satellites demonstrates strong performance, offering a novel technical approach for health assessment and advancing the development of drag-free satellite technology. Future work will focus on further optimizing the model to accommodate more complex space environments and meet higher assessment requirements.

Acknowledgements

This research was supported by National Key R&D Program of China: Gravitational Wave Detection Project (No.2021YFC2202600, No.2021YFC2202603, No.2024YFC2207900) , National Natural Science Foundation of China (No.12372048, No.12172288, No.12472046) and China Postdoctoral Science Foundation (No.2023M742835).

Reference

[1] H. L, X. S, Q. H, P. W, et al. Robust Fault Detection for Micro Thrusters of Drag-Free Satellites. 2023 China Automation Congress (CAC), 2023: 3153-3158.

[2] Lange B O, Astronautics S U D O, Engineering S U D O, Administration U S N A. The Control and Use of Drag-free Satellites. Stanford University, 1964.

[3] W Zhenhua. Research on Fault Diagnosis Approach for Attitude Control System of Satellite. Harbin Institute of Technology, 2010.

[4] T Yifan, D Liqian, J Chunhui, L Wenjing, et al. Deep Transfer Learning-Based Fault Diagnosis of Spacecraft Attitude System. Aerospace Control and Application, 2021, 47(3): 57-63.

[5] F Yidi, W Pengcheng, L Wei, A Ke, et al. Robust Controller Design for Drag-Free Satellites with Two Test Masses. Journal of Deep Space Exploration, 2023, 10(3): 310-321.

[6] B Cheng, Y Xiaokui, D Zhaohui, D Yibo. Fault diagnosis of attitude control sensors for drag-free satellite with single test mass. Aerospace Technology, 2023,(06): 1-13.

[7] Y Li, W Shuyi. A review on development of intelligent health management technology for spacecraft control systems. Acta Aeronautica et Astronautica Sinica, 2021, 42(4): 122-136.

[8] Abdelghafar S, Darwish A, Hassanien A E. Intelligent health monitoring systems for space missions based on data mining techniques. Machine learning and data mining in aerospace technology, 2020: 65-78.

[9] W Jianjun, X Hao. Study and Implementation of Spacecraft Health Management Technology. Chinese Aerospace Safety Symposium, 2017: 363-372.

[10] W Bo. Research on Methods and Application of Health Assessment. Computer Measurement ＆ Control, 2009, 17(12): 2345-2347.

[11] X Kaixin. Research on Autonomous Health State Assessment Method of Micro-Satellite . Harbin Institute of Technology, 2016.

[12] L Zheng. Research on Assessment Methods of Health Status for On-orbit Satellite. National University of Defense Technology, 2017.

[13] F Wenjing, P Yuqian, B Dongwei, G Jia, et al. Application of Analytical Hierarchy Process in Spacecraft Health Evaluation. Spacecraft Engineering, 2014, 23(2): 12-18.

[14] Li E, Li Y, Li T, Li J, et al. Intelligent analysis algorithm for satellite health under time-varying and extremely high thermal loads. Entropy, 2019, 21(10): 983.

[15] H Weigang, L Junlian, S Jin, L Xiang, et al. Health Assessment Method of Multi-level Spacecraft Control System. Aerospace Control, 2023, 41(6): 63-68.

[16] S Fei, Q Shiyin. On-orbit real-time health assessment of satellite attitude control system. Journal of Beijing University of Aeronautics and Astronautics, 2014, 40(11): 1581-1588.

ISSN:3007-9640 DOI: https://doi.org/10.70114/acmsr.2025.2.1.P221
[17] Mukhachev P A, Sadretdinov T R, Pritykin D A, Ivanov A B, et al. Modern Machine Learning Methods for Telemetry-Based Spacecraft Health Monitoring. Automation and Remote Control, 2021, 82(8): 1293-1320.

[18] B M T A, C L F, D P D, E G D. On applying AI-driven flight data analysis for operational spacecraft model-based diagnostics - ScienceDirect. Annual Reviews in Control, 2020, 49: 197-211.

[19] Liu Q, Wang C, Wang Q. Bayesian Uncertainty Inferencing for Fault Diagnosis of Intelligent Instruments in IoT Systems. Applied Sciences (2076-3417), 2023, 13(9).

[20] Z Liyuan. The Spacecraft Health Management System Based on Bayesian Networks. Harbin Institute of Technology.

[21] D Jing, Z Ping, L Xingshan, Y Jinsong. Research on Health Assessment of Integrated Vehicle Health Management. Journal of Astronautics, 2009, 30(4): 1711-1721.

[22] G Bo, W Xiaole, L Xiaoying, Z Jing. Health state assessment method based on Logistic regression model. The 11 th China Satellite Navigation Conference, 2020: 66-71.

[23] B J Y A, A Y S, A D T, C J D. A Digital Twin approach based on nonparametric Bayesian network for complex system health monitoring. Journal of Manufacturing Systems, 2021, 58: 293-304.

[24] Codetta-Raiteri D, Portinale L. Dynamic Bayesian Networks for Fault Detection, Identification, and Recovery in Autonomous Spacecraft. IEEE Transactions on Systems Man & Cybernetics Systems, 2014, 45(1): 13-24.

[25] Li C, Mahadevan S, Ling Y, Choze S, et al. Dynamic Bayesian Network for Aircraft Wing Health Monitoring Digital Twin. AIAA Journal, 2017, 55(3): 1-12.

[26] L Haisheng, G Peipei, Z Heng. Research on the Health State Assessment Method of Navigation Satellite Based on Data Fusion. China Satellite Navigation Conference, 2018: 95-99.

[27] Schumann J, Mengshoel O J, Mbaya T. Integrated Software and Sensor Health Management for Small Spacecraft. IEEE, 2011.

[28] Barua, Amitabh, Khorasani, Khashayar. Hierarchical Fault Diagnosis and Health Monitoring in Satellites Formation Flight. IEEE Transactions on Systems, Man & Cybernetics: Part C - Applications & Reviews, 2011.

[29] L Zhixiang. Research on the Drag-free Control and Simulation for A Spacecraft with Two Test Masses. Huazhong University of Science and Technology, 2021.

[30] W Shaoxin. Research on the Construction of the Sensitive Structure and Ground Evaluation Method of Space Inertial Sensor. University of Chinese Academy of Sciences, 2020.

[31] L Hongyin, L Yanchong, W Chengrui, B Yanzheng, et al. Preliminary design consideration and development of TianQin inertial sensor. Acta Scientiarum Naturalium Universitatis Sunyatseni, 2021, 60(Z1): 186-193.

[32] X Yonghao. Research on Low-frequency Noise Suppression of AC Actuator Time-sharing Control Drive Circuits for Spatial Inertial Sensors. Northeast Forestry University, 2023.

[33] X Mengting. Analysis of the Impact of Major Environmental Disturbances on Space Gravitational Reference Sensor——LISA Pathfinder to LISA. Huazhong University of Science and Technology, 2020.

[34] H Deqiang, Y Yi, H Chongzhao. Advances in DS evidence theory and related discussions. Control and Decision, 2014, 29(01): 1-11.

[35] Cheng J, Greiner R, Kelly J, Bell D A, et al. Learning Bayesian Networks from Data: An Information-Theory BasedApproach. Artificial Intelligence, 2002, 137(1-2): 43-90.

[36] Bishop C M, Nasrabadi N M. Pattern recognition and machine learning. Springer, 2006.